Full Length Article

Highly sensitive and selective gas sensors based on 2D/3D Bi$_2$MoO$_6$ micro-nano composites for trimethylamine biomarker detection

Kaidi Wu [a,b], Xiaoxi He [a], Ahmadou Ly [c], Driss Lahem [c], Marc Debliquy [b], Chao Zhang [a,*]

[a] College of Mechanical Engineering, Yangzhou University, Yangzhou 225127, PR China
[b] Service de Science des Matériaux, Faculté Polytechnique, Université de Mons, Mons 7000, Belgium
[c] Material Science Department, Materia Nova ASBL, Mons 7000, Belgium

ARTICLE INFO

ABSTRACT

Metal oxide semiconductor based gas sensors have been verified to be an effective way for food quality detection. However, the high operating temperature, insufficient sensitivity, and selectivity limit their wide application. Herein, one simplest Aurivillius oxide, Bi$_2$MoO$_6$ microspheres and a series of exfoliated g-C$_3$N$_4$/Bi$_2$MoO$_6$ hetero-composites were developed using a facile solvothermal route, which are used to detect trimethylamine (TMA, a volatile biomarker of fish freshness) at 22 °C. The introduction of E-g-C$_3$N$_4$ contributes to modulating the grain size of Bi$_2$MoO$_6$ and tuning the Bi/Mo cations valence states, thus improving the surface reactivity and electron transfer efficiency. Benefiting from the synergetic engineering of 2D/3D micro-nanostructure, crystal defects, and well-defined n-n heterojunctions, 1 wt% E-g-C$_3$N$_4$/Bi$_2$MoO$_6$ attained superior TMA sensing performance at 22 °C, including the highest response (R$_a$/R$_g$ = 10.6 @ 20 ppm) and accelerated response/recovery speed, fine selectivity, and low detection limit (1.3 ppm), which is far satisfied with the detection requirement. Furthermore, the comprehensive evaluation based on the fish color and tissue state, sensing characteristics, PCA, and pH testing results reveal the fabricated TMA sensor can achieve rapid and non-destructive fish freshness detection. This work provides insights into designing low-power consumption chemiresistive gas sensors and devices with valid practicality.

1. Introduction

Fish is not only delicious food but also rich in many nutrients [1]. However, at present, fish and other aquatic products are mainly sold live or fresh. In the process of transportation or market sales, they are prone to spoilage and cause economic losses. Additionally, accidental ingestion of stale fish can cause human foodborne poisoning and seriously affect the health of consumers [2]. Freshness is an important characteristic of fish quality. Hence, many non-destructive techniques have been used to determine fish freshness, including near-infrared spectroscopy (NIRS), hyperspectral imaging (HSI), multi-spectral imaging (MSI), and nuclear magnetic resonance (NMR) [3,4]. Although these methods can provide partially accurate information about fish freshness, the existing limitations make them unsuitable for real-time assessment of fish quality from a consumer's perspective or on the spot. Therefore, one of the alternative methods is to develop reliable and rapid detection techniques to assess fish quality in real time.

According to international standards, the concentration of volatile organic compounds biomarkers released from deteriorated sea fish can be used to evaluate fish freshness.[5]. Among them, TMA (concentration: >10 ppm level) is recommended as a kind of biomarker for sea fish freshness assessment [6,7]. Several methods were developed for TMA detection, such as quartz crystal resonator, conductometric oxide based sensors, and enzymatic based biosensor [5,8]. Notably, metal oxide semiconductor resistive (MOSR) gas sensor is a rapid, accurate, and low-cost detection technique, such as MoO$_3$, WO$_3$, α-Fe$_2$O$_3$, Co$_3$O$_4$, and In$_2$O$_3$ [9–13]. However, MOSR gas sensors still face the challenges of high working temperatures and insufficient detection limit, which will cause poor operation stability and limit their practical application. Hence, room temperature TMA sensors with high performance have attracted attention and have been developed for new-generation detection devices [14].

To realize the excellent sensing properties working at room temperature, the activated energy of molecules (redox reaction efficiency) and the mobility of electrons/ions (charge transfer) need to be improved [15]. Besides morphology control, catalyst (metal ions, metal oxides,

---

* Corresponding author at: College of Mechanical Engineering, Yangzhou University, Yangzhou 225127, Jiangsu Province, PR China.
E-mail address: zhangc@yzu.edu.cn (C. Zhang).

etc.) decoration, and incorporation with the secondary phase, developing new sensing nanomaterials is also a key and effective path [16–18]. Bi_2MoO_6, as one simplest Aurivillius oxide, possesses alternating $[BiO]^+$ layers and octahedral $[MoO_4]^{2-}$ perovskite layers. Benefiting from the unique layered structure (generating built-in electric field), Lewis acid sites, and narrow band gap (2.5–2.7 eV), improved electron mobility and reaction kinetics can be obtained [19,20]. Though there are few reports on Aurivillius oxides sensors, especially low-power consumption and high-precision gas sensors, the tunable bimetallic Bi_2MoO_6 will show great application prospects in low or room-temperature gas sensors, which needs to be systematically investigated.

Graphitic Carbon Nitride (g-C_3N_4), known as a metal-free layered two-dimensional conjugated polymer with a bandgap of around 2.7 eV (~460 nm), has a strong oxygen absorption capacity [21,22]. Therefore, g-C_3N_4 has been researched as room-temperature gas sensors. For instance, Reddeppa et al. developed g-C_3N_4/GaN nanorods gas sensor, showing a fine sensing performance to 0.5–5 ppm NO_2 at 27 °C [23]. Wang et al. reported the g-C_3N_4/WO_3 nanocomposite based acetone sensor and confirmed the sensitization effect of g-C_3N_4 nanosheets [24]. The above studies proved that introducing g-C_3N_4 will contribute to accelerating carrier transfer and improving surface activity in the electrical system. Other studies have also shown that the exfoliation improved the surface area and pore volume of g-C_3N_4 [25].

Until now, there is no reported work about Bi_2MoO_6 based gas sensors working at room temperature. Accordingly, we developed 3D Bi_2MoO_6 microspheres and 2D/3D E-g-C_3N_4/Bi_2MoO_6 nanocomposites with oxygen vacancies and well-defined n-n heterojunction structures using a solvothermal synthesis method. The microstructural and gas sensing characteristics of the as-fabricated gas sensors were investigated. Benefiting from the hierarchical nanostructure, large oxygen adsorption capacity, and accelerated carriers migration, the prepared E-g-C_3N_4/Bi_2MoO_6-based TMA sensors showed high responses (R_a/R_g = 10.6 @ 20 ppm), short response/recovery time, and a low detection limit (1.3 ppm). Furthermore, the sea fish freshness detection test using the fabricated gas sensor was conducted to identify the practical application potential. This simple strategy will provide a guide to designing room-temperature gas sensors for the development of simple and rapid fish freshness detection devices.

2. Experimental section

The preparation procedures of exfoliated g-C_3N_4 can be found in the Supplementary Material.

2.1. Synthesis of E-g-C_3N_4/Bi_2MoO_6 composites

All chemical reagents (VWR Belgium) were used without further purification. Bi_2MoO_6 microspheres and E-g-C_3N_4/Bi_2MoO_6 composites were synthesized as follows: 10 mL ethylene glycol (EG) and 20 mL ethanol were first added into a 200 mL beaker, then the E-g-C_3N_4 with a certain mass was mixed in the above beaker. Then the suspension in the beaker was sonicated for 10 min. Subsequently, 2 mmol $Na_2MoO_4·2H_2O$, and 4 mmol $Bi(NO_3)_3·5H_2O$ were added into the suspension. After magnetically stirring for 1 h, the obtained suspension was transferred into a Teflon- stainless steel autoclave (100 mL), which was heated under 160 °C for 24 h. The products were washed 5 times with deionized water and anhydrous ethanol, then dried at 80 °C for 12 h. These samples with E-g-C_3N_4 of 0, 6.1 mg, 12.2 mg, 36.6 mg, and 61.0 mg are denoted as Bi_2MoO_6, 0.5 wt% E-g-C_3N_4/Bi_2MoO_6, 1 wt% E-g-C_3N_4/Bi_2MoO_6, 3 wt% E-g-C_3N_4/Bi_2MoO_6 and 5 wt% E-g-C_3N_4/Bi_2MoO_6.

2.2. Characterization

The phase structure of all powders was investigated by X-ray diffraction (XRD, Siemens/Bruker D-5000) using Co-Kα_1 radiation (λ =

1.7889 Å). The morphology was observed using field-emission scanning electron microscopy (FESEM, SU8020 Hitachi). EDX was used to detect the elements distributions of C, N, Bi, Mo, and O in the final products. The surface element states were determined using X-ray photoelectron spectroscopy (XPS, XPS Phi Versa Probe 5000). The FT-IR test was carried out by an IFS 66 v/s FTIR spectrometer (Bruker). UV–vis diffuse reflectance spectrophotometer (Cary 5000, Varian) was used to determine the optical bandgap of all samples. The specific surface area of the samples was measured by Brunauer-Emmett-Teller (BET) method (FlowSorb III 2310, Micromeritics). The test was carried out at 77 K with nitrogen.

2.3. Fabrication and measurement of gas sensors

The paste was prepared by mixing the powders with deionized water, then it was coated onto the Al_2O_3 substrate. These gas sensors (Fig. S1) were obtained after being kept at 120 °C for 24 h. The room temperature (22 ± 2 °C) gas sensors testing system is displayed in Fig. S1. More testing information can also be found in Supplementary Material. The n-type response of Bi_2MoO_6 based gas sensors is defined as R_a/R_g, where R_a and R_g represent the stable resistance values in air and target gas, respectively.). The response/recovery time is taken from the time when the total resistance change reaches 90%.

2.4. Determination of pH

Cod fish was bought from the local market of Mons. The samples (0.6 g) under different storage periods were mixed with 6 mL distilled water to form homogenate suspensions. The pH values of these suspensions were tested using a digital pH meter (pH 1100 L, VWR).

2.5. Determination of fish freshness

The fabricated 1 wt% E-g-C_3N_4/Bi_2MoO_6 based TMA gas sensor was used to detect the freshness of real fish. The fish fillet (fresh *Cod* fish, 20 g) was defrosted and was then placed in a sealed bottle (0.3 L) at around 23 °C. During the whole detection procedure, the total gas flow was kept at 500 mL/min. The sensor electrical resistance variation towards fish of different storage periods (1, 2, 3, 4, 5, and 8 days) was recorded, and PCA, color & tissue state, and pH change were used to classify and assess the fish freshness.

3. Results and discussion

3.1. Structural and morphological characteristics

The diagram in Fig. 1 a-b illustrates the preparation procedures of exfoliated g-C_3N_4 nanosheets and 2D/3D E-g-C_3N_4/Bi_2MoO_6 heterocomposites. Fig. 1c displays the schematic diagram of as-fabricated gas sensors, which were used to determine the phase structures of the sensing materials by XRD. In Fig. 1d, the bulk and exfoliated g-C_3N_4 show the characteristic peaks at around 27.6°, which are indexed to the (0 0 2) plane of g-C_3N_4 (JCPDS No. 87-1526). Notably, the (0 0 2) plane is from the inter-layer stacking of conjugated aromatic systems in g-C_3N_4. The peak intensity of the (0 0 2) plane decreased by 43.6%, revealing the nanosheets have been exfoliated successfully from bulk g-C_3N_4 [26]. The inset photographs show the bulk g-C_3N_4 suspension was white after being ultrasonicated for 15 min, while the E-g-C_3N_4 suspension changed to transparent. And a red laser light was passed through it, this Tyndall effect further confirmed the existence of nanosized materials [27]. In Fig. 1e, the characteristic peaks of the samples that can be observed at 20–80° are matched to the orthorhombic Bi_2MoO_6 (JCPDS-84-0787). Because of the small amounts of E-g-C_3N_4, the XRD profiles of E-g-C_3N_4/Bi_2MoO_6 composites mainly show the peaks of Bi_2MoO_6. Additionally, there are several detected peaks corresponding to the Al_2O_3 substrate. The average grain sizes of pristine Bi_2MoO_6 and E-g-C_3N_4/Bi_2MoO_6
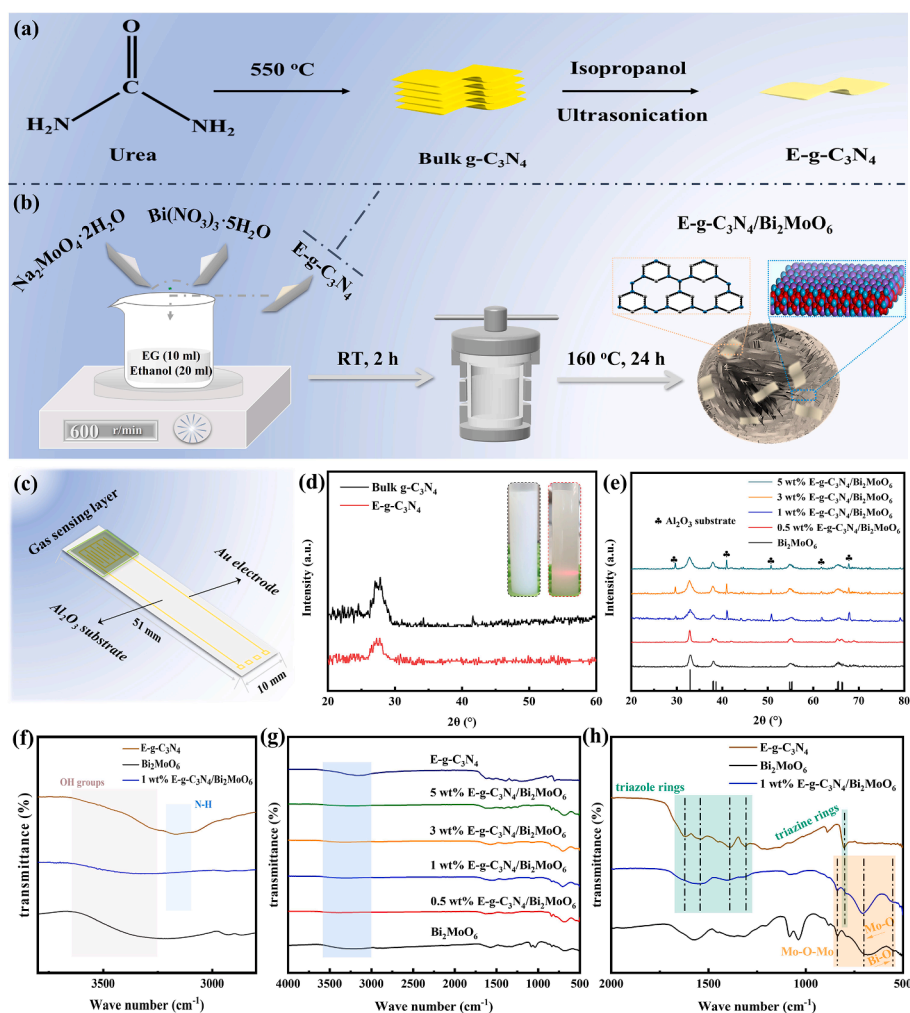
Fig. 1. Synthesis procedures of (a) exfoliated g-C₃N₄ and (b) E-g-C₃N₄/Bi₂MoO₆ composites. (c) The schematic diagram of the fabricated gas sensor. XRD patterns of (d) bulk g-C₃N₄ and E-g-C₃N₄ in 20-60° and (e) pristine Bi₂MoO₆ microspheres and E-g-C₃N₄/Bi₂MoO₆ composites. Insets are photographs of bulk g-C₃N₄ and E-g-C₃N₄ suspensions in water. (f-h) FT-IR curves of exfoliated g-C₃N₄, Bi₂MoO₆, and E-g-C₃N₄/Bi₂MoO₆ composites.

composites were confirmed using the Debye-Scherrer equation: $D = 0.89\lambda/\beta\cos\theta$, where λ is the wavelength of the Co Kα radiation ($\lambda = 0.17889$ nm), β is the peak width at half maximum (FWHM) of identified crystal planes, and θ is the position of XRD peaks. The grain sizes were estimated as 16.0 nm, 11.2 nm, 7.4 nm, 9.2 nm, and 12.3 nm, respectively.

The chemical bonds of as-synthesized E-g-C₃N₄, Bi₂MoO₆, and E-g-C₃N₄/Bi₂MoO₆ composites were investigated using FT-IR spectra (Fig. 1g-h). In the spectrum of Bi₂MoO₆, three peaks at 553.4, 701.8, and 839.9 cm^{-1} are indexed to the stretching of Bi-O, stretching vibrations of Mo-O and the bridging stretching vibrations of Mo-O-Mo bond, respectively [28,29]. For E-g-C₃N₄, the peak at 801.3 cm^{-1} is attributed to the triazine rings, while the peaks in the range of 1200–1700 cm^{-1} belong to the C-N heterocycles of triazole rings stretching. The peaks from 3100 cm^{-1} to 3600 cm^{-1} indicate the residual -NH$_x$ and adsorbed hydroxyl groups [21]. Meanwhile, the characteristic peaks of E-g-C₃N₄ and Bi₂MoO₆ could be found in all E-g-C₃N₄/Bi₂MoO₆ nanocomposites, thereby further supporting the construction of the hetero-composites.

The effect of the introduction of E-g-C₃N₄ on the band gap of the composites was investigated. UV–vis diffuse reflection spectra were firstly obtained (Fig. S2a), then the band gaps of all samples were estimated using Kubelka-Munk formula: $(F(R)h\nu)^{1/n} = K/S = (1-R)^2/2R = B$ $(h\nu-E_g)$, where the K is absorption coefficient, S is the reflection coefficient, R is reflectivity (%), h is Planck's constant, ν is the frequency of the light, E_g is a physical quantity related to the material [30]. As shown in

Fig. S2b, the bandgap values of Bi₂MoO₆ and E-g-C₃N₄ were approximately 2.55 eV and 2.88 eV. Meanwhile, the E-g-C₃N₄/Bi₂MoO₆ composites exhibit increased band gap values of 2.58 eV, 2.61 eV, 2.65 eV, and 2.67 eV, respectively, which might be due to the synergistic effect of n-n junction in the E-g-C₃N₄/Bi₂MoO₆.

The morphology of the bulk E-g-C₃N₄, E-g-C₃N₄, Bi₂MoO₆, and E-g-C₃N₄/Bi₂MoO₆ composites was characterized using FE-SEM. In Fig. 2c-d, E-g-C₃N₄ showed a cluster of 5–10 μm and wrinkled nanosheets (thickness: ~35 nm), while bulk g-C₃N₄ showed a larger size (Fig. 2a-b). Fig. 2e and f show that Bi₂MoO₆ presents a hierarchical spherical structure, and the microspheres are assembled with crossed nanosheets. In Fig. 2g-n, when the E-g-C₃N₄ was introduced, the composites still maintain a micro-spherical structure, and the E-g- C₃N₄ nanosheets are loaded on the surface of Bi₂MoO₆, making the surface rougher. Fig. 2o shows the magnified image of 1 wt% E-g-C₃N₄/Bi₂MoO₆ composite and its schematical diagram, which consists of E-g-C₃N₄ and orthorhombic Bi₂MoO₆. Additionally, Fig. S3 shows the surface EDS elemental maps observed in the four E-g-C₃N₄/Bi₂MoO₆ composites samples. The results indicate the co-existence of C, N, Bi, Mo, and O, and the increased content of N suggests that E-g-C₃N₄ of various mass fractions were successfully compounded with the Bi₂MoO₆.

The surface elemental compositions of pristine Bi₂MoO₆, E-g-C₃N₄, and 1 wt% E-g-C₃N₄/Bi₂MoO₆ were elucidated through XPS. Fig. S4 shows the full survey spectrum, confirming the co-existence of Bi₂MoO₆ and g-C₃N₄ in 1 wt% E-g-C₃N₄/Bi₂MoO₆ composite. As shown in Fig. 3a,
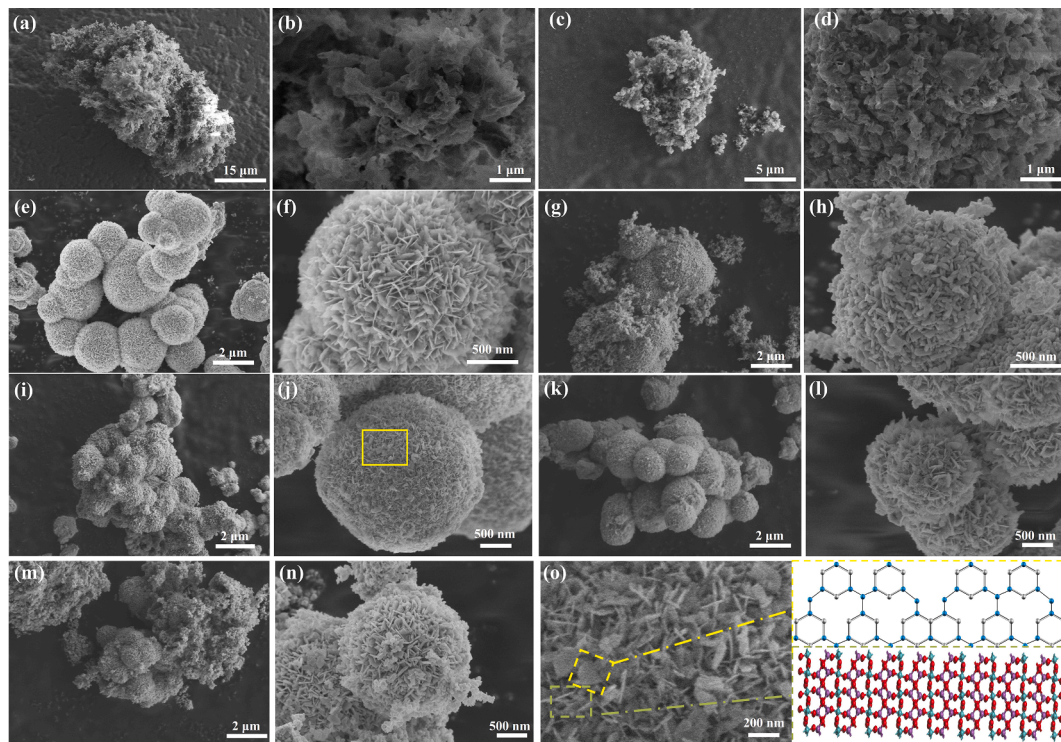
Fig. 2. FE-SEM images of (a, b) Bulk g-C$_3$N$_4$, (c, d) E-g-C$_3$N$_4$, (e, f) pristine Bi$_2$MoO$_6$ microspheres, (g, h) 0.5 wt% E-g-C$_3$N$_4$/Bi$_2$MoO$_6$, (i, j) 1 wt% E-g-C$_3$N$_4$/Bi$_2$MoO$_6$, (k, l) 3 wt% E-g-C$_3$N$_4$/Bi$_2$MoO$_6$, (m, n) 5 wt% E-g-C$_3$N$_4$/Bi$_2$MoO$_6$ composites. (o) Enlarged FE-SEM image of 1 wt% E-g-C$_3$N$_4$/Bi$_2$MoO$_6$ and its schematical diagram of E-g-C$_3$N$_4$ and orthorhombic Bi$_2$MoO$_6$.
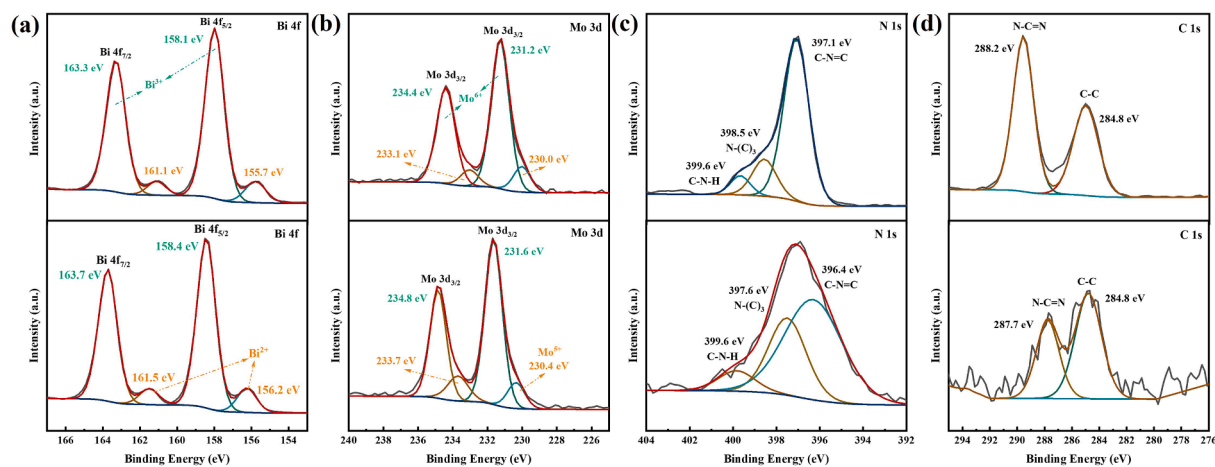
Fig. 3. Elements chemical states of pristine Bi$_2$MoO$_6$, E-g-C$_3$N$_4$ and 1 wt% E-g-C$_3$N$_4$/Bi$_2$MoO$_6$ determined via XPS: (a) Bi 4f and (b) Mo 3d of pristine Bi$_2$MoO$_6$ and 1 wt% E-g-C$_3$N$_4$/Bi$_2$MoO$_6$, (c) N 1s and (d) C 1s of pristine E-g-C$_3$N$_4$ and 1 wt% E-g-C$_3$N$_4$/Bi$_2$MoO$_6$.

the two peaks located at 158.1 and 163.3 eV in Bi$_2$MoO$_6$ spectra are ascribed to Bi 4f$_{7/2}$ and Bi 4f$_{5/2}$, respectively [31]. And the two tiny peaks at 155.7 and 161.1 eV are ascribed to Bi^{2+} in Bi$_2$MoO$_6$ [32,33]. Notably, these two similar sets of peaks can also be observed in 1 wt% E-g-C$_3$N$_4$/Bi$_2$MoO$_6$, revealing the existence of Bi^{3+} and Bi^{2+} in both powders. As shown in Fig. 3b, the peaks at 234.5 eV and 231.3 eV are assigned to Mo 3d$_{3/2}$ and Mo 3d$_{5/2}$ in Bi$_2$MoO$_6$, corresponding to the Mo^{6+} in Bi$_2$MoO$_6$ [28,31]. Additionally, the specific peaks at the binding energies of 233.1 eV and 230.0 eV are attributed to Mo^{5+} [34]. The generation of low valence Bi and Mo elements could be ascribed to the electron reconstruction in [BiO]$^+$-[MoO$_4$]$^{2-}$-[BiO]$^+$ layers, which are also related to the formation of oxygen vacancies. More details will be discussed in the gas sensing mechanism. In Fig. 3c, the g-C$_3$N$_4$ shows

three obvious peaks, among which 397.1 eV represents sp^2-bonded N atoms in C-N=C, 398.5 eV represents N-(C)$_3$ group, and 399.7 eV corresponds to NH$_2$-functionalized groups (C-N-H), respectively [35,36]. Compared to g-C$_3$N$_4$, all the peaks of 1 wt% E-g-C$_3$N$_4$/Bi$_2$MoO$_6$ nanocomposite shifted toward lower binding energies of 396.4, 397.6, and 399.6 eV. In Fig. 3d, the peaks of the C1s in g-C$_3$N$_4$ at the binding energies of 284.8 and 288.2 eV correspond to sp^3-coordinated C, and sp^2 hybridized C from the N-C=N bond, respectively [37,38]. For 1 wt% E-g-C$_3$N$_4$/Bi$_2$MoO$_6$, all the peaks of 1 wt% E-g-C$_3$N$_4$/Bi$_2$MoO$_6$ nanocomposite also show a shift toward lower binding energies of 284.8 and 287.7 eV. Notably, the Bi 4f and Mo 3d peaks of the composite show a slight shift towards the higher binding energies, while the main peaks of C 1s and N 1s show a slight shift to lower binding energies, indicating the

transfer of electrons between g-C_3N_4 and Bi_2MoO_6 [28,29].

The specific surface areas were determined using Brunauer-Emmett-Teller (BET) method. As shown in Table S1, the specific surface areas of pristine Bi_2MoO_6, 1 wt% E-g-C_3N_4/Bi_2MoO_6 and 3 wt% E-g-C_3N_4/Bi_2MoO_6 were 17.69, 46.16 and 34.84 m^2g^{-1}. According to the reported literature [15], the specific surface area is related to grain size (A = 6/D*ρ, where A is the specific surface area, D is the grain size, and ρ is the density of the crystal), suggesting that specific surface area will decrease with increasing grain size. Hence, the determined specific surface areas of samples are consistent with the change of grain sizes, and 1 wt% E-g-C_3N_4/Bi_2MoO_6 obtained the largest specific surface area, which will contribute to enhancing gas sensing properties.

3.2. Gas sensing performance

Pristine Bi_2MoO_6 microspheres and E-g-C_3N_4/Bi_2MoO_6 composites-based gas sensors were evaluated at room temperature. The dynamic resistance variations of all gas sensors towards 5–20 ppm TMA are depicted in Fig. S5. Notably, the pristine E-g-C_3N_4 nanosheets showed barely response to TMA of 5–20 ppm. Fig. S6a-e shows the corresponding dynamic response curves. The series of E-g-C_3N_4/Bi_2MoO_6 composites present significantly higher response values than that of pristine Bi_2MoO_6 microspheres and E-g-C_3N_4 nanosheets. As shown in

Fig. S6f, the 1 wt% E-g-C_3N_4/Bi_2MoO_6 showed the highest response to 5–20 ppm TMA at room temperature. The response values of 1 wt% E-g-C_3N_4/Bi_2MoO_6 to 5–20 ppm TMA are 2.45–10.6, while that of pristine Bi_2MoO_6 is only 1.08–1.41.

Moreover, the response/recovery speeds of pristine Bi_2MoO_6 and 1 wt% E-g-C_3N_4/Bi_2MoO_6 to 20 ppm TMA were also analyzed. As shown in Fig. 4a, the 1 wt% E-g-C_3N_4/Bi_2MoO_6 gas sensor displayed shorter time (42 s/209 s) in both response and recovery, while those of pristine Bi_2MoO_6 were 64 s and 253 s, respectively.

Selectivity is one key parameter in practical application. In Fig. 4b-c, pristine Bi_2MoO_6 microspheres and 1 wt% E-g-C_3N_4/Bi_2MoO_6 composites gas sensors were investigated using NH_3, $C_6H_{15}N$, C_2H_5OH, C_3H_6O, C_3H_8O, H_2S, and CH_3OH of 20 ppm under the same test condition. The 1 wt% E-g-C_3N_4/Bi_2MoO_6 shows a significantly higher response of 10.6 to TMA, while the response to 20 ppm NH_3, $C_6H_{15}N$, C_2H_5OH, C_3H_6O, C_3H_8O, H_2S, and CH_3OH are 4.6, 3.1, 3.2, 2.3, 1.7, 1.5, and 1.1, respectively. Additionally, pristine Bi_2MoO_6 shows a similar response to all target gases, indicating 1 wt% E-g-C_3N_4/Bi_2MoO_6 presents enhanced selectivity to TMA. Hence, 1 wt% E-g-C_3N_4/Bi_2MoO_6 sensor can detect and identify TMA effectively. The selectivity can be explained as follows: The main bond energies of target gases are TMA & TEA (C-N, 307 kJ/mol), isopropanol (C-C, 345 kJ/mol), H_2S (H-S, 376 kJ/mol) NH_3 (N-H, 391 kJ/mol), methanol C-H (411 kJ/mol), ethanol (O-H, 458.8 kJ/mol),
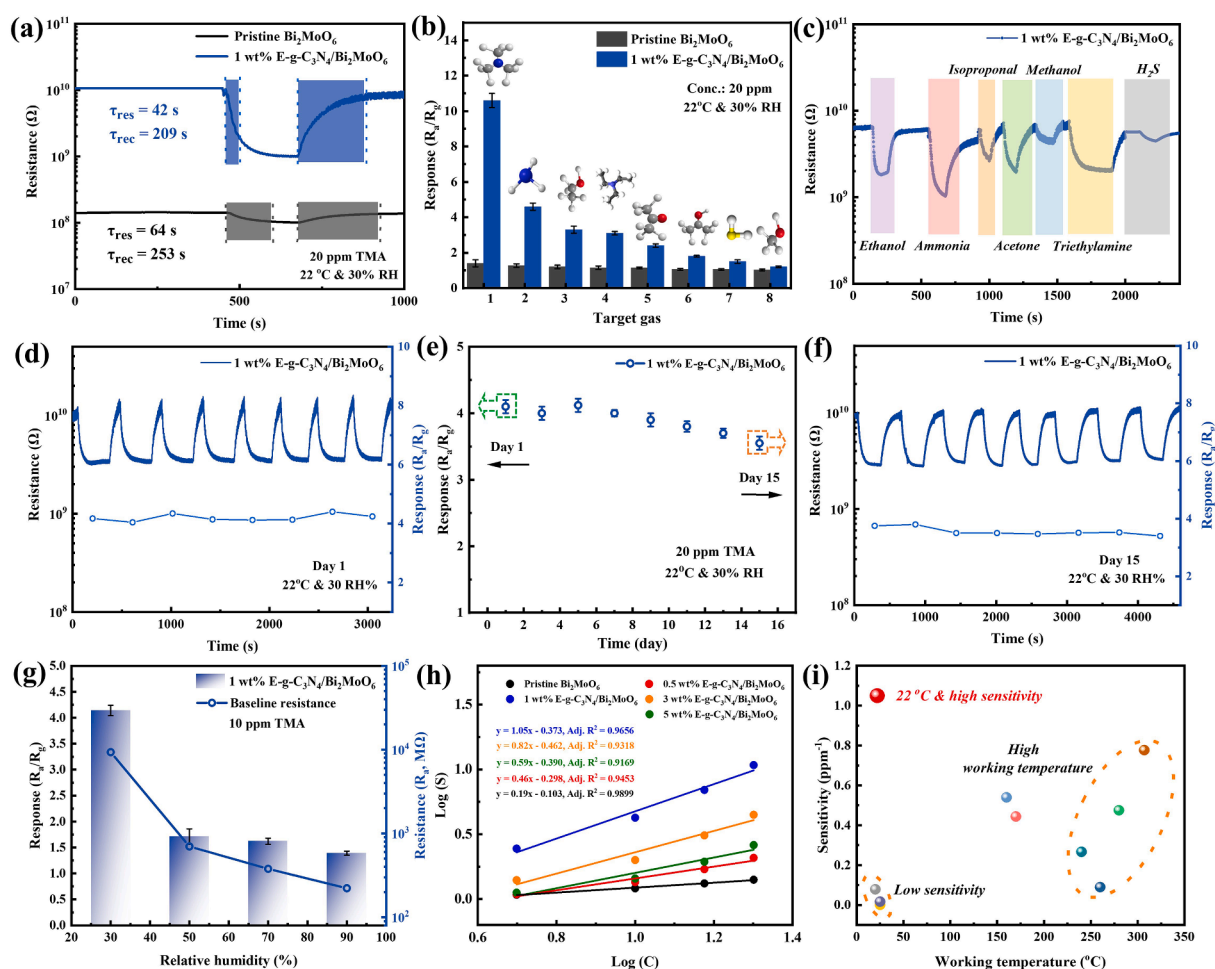

Fig. 4. (a) Responses/recovery time of pristine Bi_2MoO_6 microspheres and 1 wt% E-g-C_3N_4/Bi_2MoO_6 composites to 20 ppm TMA at room temperature. (b, c) Selectivity to 20 ppm TMA and other interfering gases of pristine Bi_2MoO_6 microspheres and E-g-C_3N_4/Bi_2MoO_6 composites. (d) Response to 20 ppm TMA of 1 wt% E-g-C_3N_4/Bi_2MoO_6 in Day 1. (e) Response stable characteristics of 1 wt% E-g-C_3N_4/Bi_2MoO_6 sensor to 20 ppm TMA in 15 days. (f) response to 20 ppm TMA of 1 wt% E-g-C_3N_4/Bi_2MoO_6 in Day 15. (g) Variation of baseline resistance and response values of 1 wt% E-g-C_3N_4/Bi_2MoO_6 versus relative humidity. (h) Linear relation between Log (S) and Log (C) of all sensors. (i) Comparison of the TMA sensitivity between this work (red) and recently reported metal oxides-based gas sensors (others). (For interpretation of the references to color in this figure legend, the reader is referred to the web version of this article.)

and acetone (C=O, 798.9 kJ/mol) [39,40]. In addition, Bi_2MoO_6 has enough Lewis acid sites, which can easily detect alkaline gases. In general, the more alkyl groups attached to a nitrogen atom, the more alkaline it is. However, the increase of the alkyl group also leads to the increase of the steric hindrance, and it is difficult for the proton to approach the electron pair of the amine nitrogen, so the alkaline weakens. Therefore, the sensor was more sensitive to TMA because of its stronger alkaline. The similar results can also be found in the previous work [41]. The reproducibility and long-term operation stability of gas sensor were also evaluated. Fig. 4d-f display the continuous sensing behavior of 1 wt% E-g-C_3N_4/Bi_2MoO_6 towards 10 ppm TMA in five cycles, showing the stable response values of around 4.0. Fig. 4e displayed the stable response values of 1 wt% E-g-C_3N_4/Bi_2MoO_6 towards 10 ppm TMA in 15 days, revealing the fabricated gas sensor attained good operating stability.

The sensing properties of room temperature gas sensors may be affected by the change in relative humidity. Hence, the response of 1 wt% E-g-C_3N_4/Bi_2MoO_6 to TMA was tested in 30–90 RH%. Fig. 4g displays the corresponding response values towards 10 ppm TMA at different RH (30, 50, 70, and 90%), which were 4.14, 1.71, 1.62, and 1.39, respectively. With the increased relative humidity, the baseline resistance and response values of 1 wt% E-g-C_3N_4/Bi_2MoO_6 based sensor are continuously decreased. This can be explained that the water molecules exhibit electron-donating behavior, therefore, the existence of water vapor molecules will lower the baseline resistance [42]. Additionally, the adsorbed water molecules will occupy the surface active sites of 1 wt% E-g-C_3N_4/Bi_2MoO_6 and prevent TMA from reacting with the absorbed oxygens, thus declining the resistance change of the sensor caused by

TMA [43]. After the relative humidity reached a high level (70 % and 90 %), the adsorbed water molecules will gradually reach saturation, thus resulting in slight effect on the sensing properties at higher humidity levels.

As shown in Fig. 4h, 1 wt% E-g-C_3N_4/Bi_2MoO_6 presents good linear response (R^2 is 0.9656) and the highest sensitivity (1.05 ppm^{-1}). The noise of the sensor (RMS_{noise}) was calculated as 0.4643. Based on the method proposed by the International Union of Pure and Applied Chemistry (IUPAC), the limit of detection (LOD = 3 RMS_{noise}/Slope) of 1 wt% E-g-C_3N_4/Bi_2MoO_6 composite was approximately 1.3 ppm, which is enough for the practical application of seafood freshness detection [44]. Additionally, the comparison with the TMA sensing properties of recently reported metal oxides based gas sensors are shown in Fig. 4i and Table S2. 1 wt% E-g-C_3N_4/Bi_2MoO_6 composite exhibits superior room-temperature TMA sensing properties than the listed gas sensors. The gas sensor in this work will be a competitive candidate in practical application.

3.3. Gas sensing mechanisms

The gas sensing mechanisms were clarified through the chemical redox reactions occurring on the sensing material surface [45,46]. In Fig. 5a, the fabricated Bi_2MoO_6 microspheres and 1 wt% E-g-C_3N_4/Bi_2MoO_6 sensors display n-type semiconductor gas sensing characteristics. When the sensing layers encounter air, the formed chemisorbed oxygen species (O_2^-) will decrease the electron concentration and thicker the electron depletion layer at the interface, leading to high baseline resistance. Once the gas sensors are exposed to TMA, the O_2^- will react
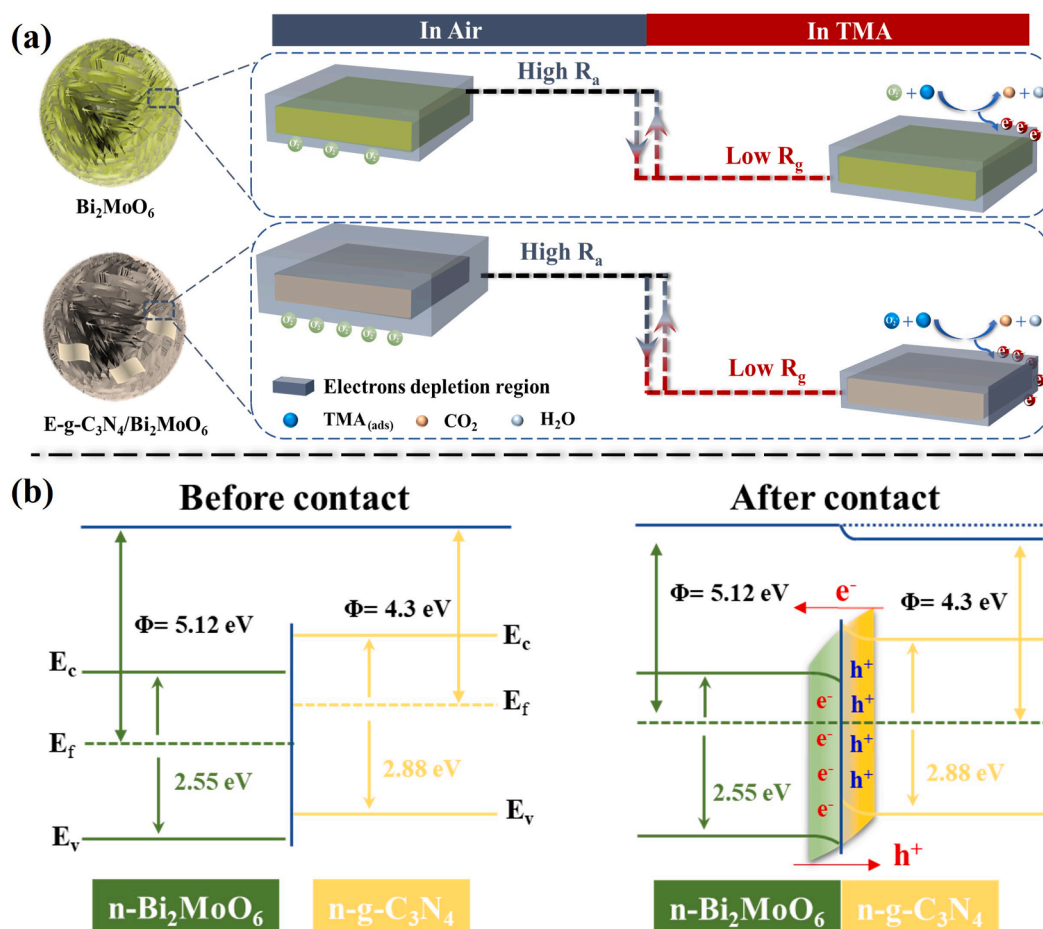

Fig. 5. (a) Adsorption and reaction model of the TMA sensing process on the surface of pristine Bi_2MoO_6 microspheres and 1 wt% E-g-C_3N_4/Bi_2MoO_6 composite-based gas sensor. (b) Energy bands model of the formation of n-n heterojunction structure.
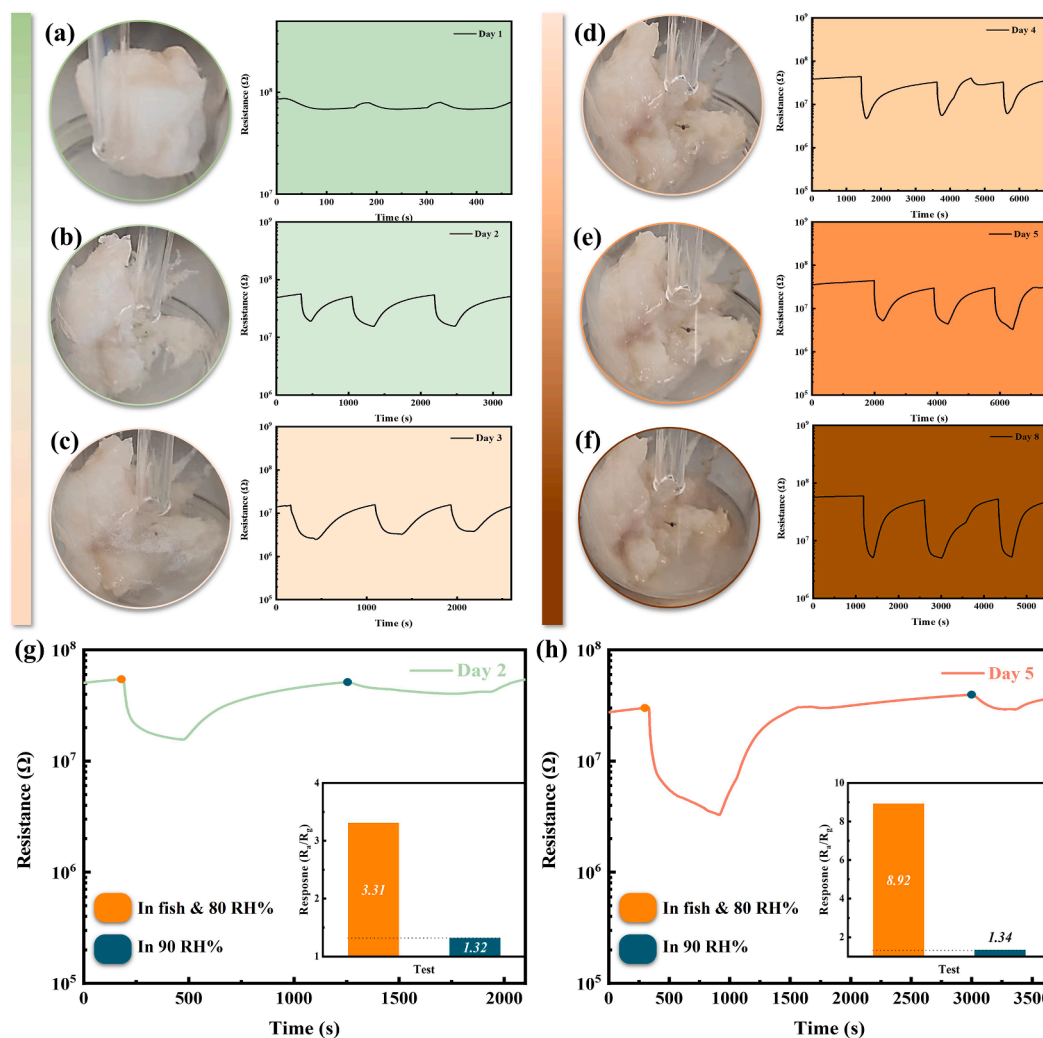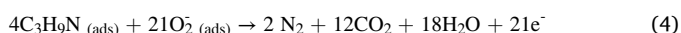
Fig. 6. (a-f) Response/recovery curves of 1 wt% E-g-C$_3$N$_4$/Bi$_2$MoO$_6$ to the spoilage volatile gas of fish stored for 1–8 days at 23 °C and the corresponding photographs of fish. (g-h) Dynamic resistance variation and response of 1 wt% E-g-C$_3$N$_4$/Bi$_2$MoO$_6$ gas sensor to the relative humidity difference during the practical detection.

with TMA and release the electrons back to the conduction bands, leading to decreased resistance. The whole sensing procedures are as Eqs. (1)–(4) [47,48].

$$O_2 \text{ (gas)} \rightarrow O_2 \text{ (ads)} \tag{1}$$

$$O_2 \text{ (ads)} + e^- \rightarrow O_2^- \text{ (ads)} \tag{2}$$

$$C_3H_9N \text{ (gas)} \rightarrow C_3H_9N \text{ (ads)} \tag{3}$$

$$4C_3H_9N \text{ (ads)} + 21O_2^- \text{ (ads)} \rightarrow 2\,N_2 + 12CO_2 + 18H_2O + 21e^- \tag{4}$$

The enhanced TMA sensing mechanisms of 1 wt% E-g-C$_3$N$_4$/Bi$_2$MoO$_6$ are explained as follows: Firstly, 1 wt% E-g-C$_3$N$_4$/Bi$_2$MoO$_6$ had the hierarchical nanostructure, contributing to facilitating the gas diffusion and providing more active sites, thus improving sensing properties [49,50], additionally, the exfoliated g-C$_3$N$_4$ will boost the charge separation and transfer efficiency [26]. Secondly, with the introduction of E-g-C$_3$N$_4$, the grain size decreased, and the specific surface area possibly become larger, which will contribute to enhancing the sensing performance. After the mass fraction of E-g-C$_3$N$_4$ exceeded 1 wt%, the grain sizes increased and the specific surface area possibly become smaller, thus resulting in lowering the sensing performance. Thirdly, besides the electronic nature of E-g-C$_3$N$_4$ and Bi$_2$MoO$_6$, the formation of n-n E-g-C$_3$N$_4$/Bi$_2$MoO$_6$ heterojunction also boosts the

sensing characteristics. The work function and bandgap of Bi$_2$MoO$_6$ are approximately 5.12 and 2.55 eV, respectively, while that of E-g-C$_3$N$_4$ are around 4.3 and 2.88 eV, respectively [21,51]. Fig. 5b depicts the energy bands diagram of the well-defined E-g-C$_3$N$_4$/Bi$_2$MoO$_6$ heterojunctions. The larger carrier depletion layer and potential barrier formed at the heterojunction interface will lead to a high baseline resistance (R$_a$), which is conducive to promoting the redox reaction between TMA and sensing materials and enhancing the sensing properties. Additionally, as shown in Fig. S8, when the sensing materials are exposed to TMA, E-g-C$_3$N$_4$/Bi$_2$MoO$_6$ will show the more significant shrink of carrier depletion layer and potential barrier height (ΔV_b). Based on the equation ($\Delta R \propto \exp\{-q\Delta V_b/k_BT\}$), where ΔR refers to the variation of resistance, T represents temperature and k_B is the Boltzmann constant.), a sharp downshift of sensor resistance (ΔR) for E-g-C$_3$N$_4$/Bi$_2$MoO$_6$ will occur, resulting from the large variation of potential barrier height, thus attaining superior sensing capacity.

Fourthly, the change of carrier concentration is a key factor in gas sensing procedures. The gas response (S) can be defined as S = R$_a$/R$_g$ = c$_g$/c$_a$ = Δc/c$_a$ + 1 [52], where c$_g$ and c$_a$ represent the electron concentration in target gas and air, Δc = c$_g$-c$_a$ is the corresponding variation. The lower the electrons concentration in air and the larger electrons concentration variation is, the higher response to the reducing gas can be. According to the results of Fig. 6 and Table S3, the O 1s spectra of all

samples can be fitted with four peaks at around 529.1, 529.8, 530.7, and 531.8 eV, corresponding to the lattice oxygen (Bi-O and Mo-O), oxygen vacancy (O_V) and chemisorbed oxygen (O_C), respectively. In 1 wt% E-g-C_3N_4/Bi_2MoO_6, the main peaks are located at 528.8, 529.7, 530.6, and 531.6 eV, respectively. The peaks shift towards the lower binding energies of O 1s is ascribed to the improved electron density around oxygen atoms, resulting from the formation of n-g-C_3N_4/n-Bi_2MoO_6 heterojunction. Additionally, the co-existence of mixed valence state Bi (Bi^{2+}/Bi^{3+}) and Mo (Mo^{5+}/Mo^{6+}) further confirmed the production of oxygen vacancies. The atom percentage of O_V and O_C of 1 wt% E-g-C_3N_4/Bi_2MoO_6 is calculated as 23.9 at%, while that of pristine Bi_2MoO_6 is 11.3 at%. The abundant O_V and O_C will contribute to making carrier depletion layer thicker (lowering the carrier concentration in air) and boosting the reaction between the sensing layer and TMA (enlarging the variation of carrier concentration).

Moreover, the experimental data corroborate the proposed enhanced sensing mechanisms. In Fig. S8, the baseline resistance and their variation of Bi_2MoO_6 and all E-g-C_3N_4/Bi_2MoO_6 composites during the response procedure were investigated again. Among them, 1 wt% E-g-C_3N_4/Bi_2MoO_6 presents the highest baseline resistance (R_a, 1.07×10^{10} Ω) and a larger variation of resistance (ΔR, 9.71×10^9 Ω), while those of Bi_2MoO_6 and other E-g-C_3N_4/Bi_2MoO_6 composites are lower and smaller. These results further identify the lower carrier concentration in air and larger electrons concentration variation in TMA of 1 wt% E-g-C_3N_4/Bi_2MoO_6, revealing that the superior gas sensing properties benefit from the unique 2D/3D micro-nanostructure, decreased grain size, oxygen vacancies, and heterojunctions.

3.4. Practical applications of E-g-C_3N_4/Bi_2MoO_6 sensor

Herein, the as-fabricated 1 wt% E-g-C_3N_4/Bi_2MoO_6 microspheres-based gas sensor was used to detect the released gases from *Cod* fish. As shown in Fig. S9, the homemade testing system was used to detect the released TMA from 20 g fish during storage for 8 days at around 23 °C. The optical photographs of *Cod* fish at different storage periods and the corresponding response/recovery transient curves of 1 wt% E-g-C_3N_4/Bi_2MoO_6 gas sensor are shown in Fig. 7a-f. The physical properties (color and softening) of fish changed (darker color and soft muscle tissue) along with the storage time, indicating the beginning and exacerbation of fish deterioration. Furthermore, the gas sensor showed larger signal variation to the released volatile gas along with the increased storage period.

Additionally, the high humidity content of the fish body may cause the humidity change in the whole test procedure, resulting in unreliable output signals. Hence, the effect of the humidity difference of the chamber on the sensor response was studied. Firstly, the relationship between the relative humidity and output voltage of the commercial humidity sensor is determined (Fig. S10). Then, the exact relative humidity of the target gas flow from the bottle with *Cod* fish fillet was determined as 90 RH% (~4.0 V) using the commercial humidity sensor. After balancing both the response and the humidity difference, the relative humidity of carrier air flow was controlled at 80 RH% during the whole test procedure. As shown in Fig. 7g-h, the response values to fish (Day 2) with 80 RH% and 90 RH% were 3.31 and 1.32, respectively, while that of fish (Day 5) were 8.92 and 1.34, respectively. Therefore, the relative humidity difference (Δ10%) always shows a similar effect on the response and baseline resistance values, especially, which shows slight influence on Day 5. Hence, the response results in Day 1–8 were used directly for the next analysis.

Fig. 8a displays the logical block diagram of the fish freshness evaluation system, the detected TMA released from 20 g fish and the corresponding pH values during the storage at room temperature were used to present the comprehensive evaluation of fish freshness. In Fig. 8b, the response values of 1 wt% E-g-C_3N_4/Bi_2MoO_6 gas sensor increased from 1.25 to 11.71 with the storage time. In addition, the response values were linearly proportional ($R^2 = 0.975$) to the storage time, indicating the quantitative and predictive analysis ability of 1 wt% E-g-C_3N_4/Bi_2MoO_6 gas sensor. In Fig. 8d, the pH decreased to 6.73 during the first 2 days, resulting from the produce lactic acid and the generation of adenosine triphosphate (ATP) and H^+ [53]. During storage
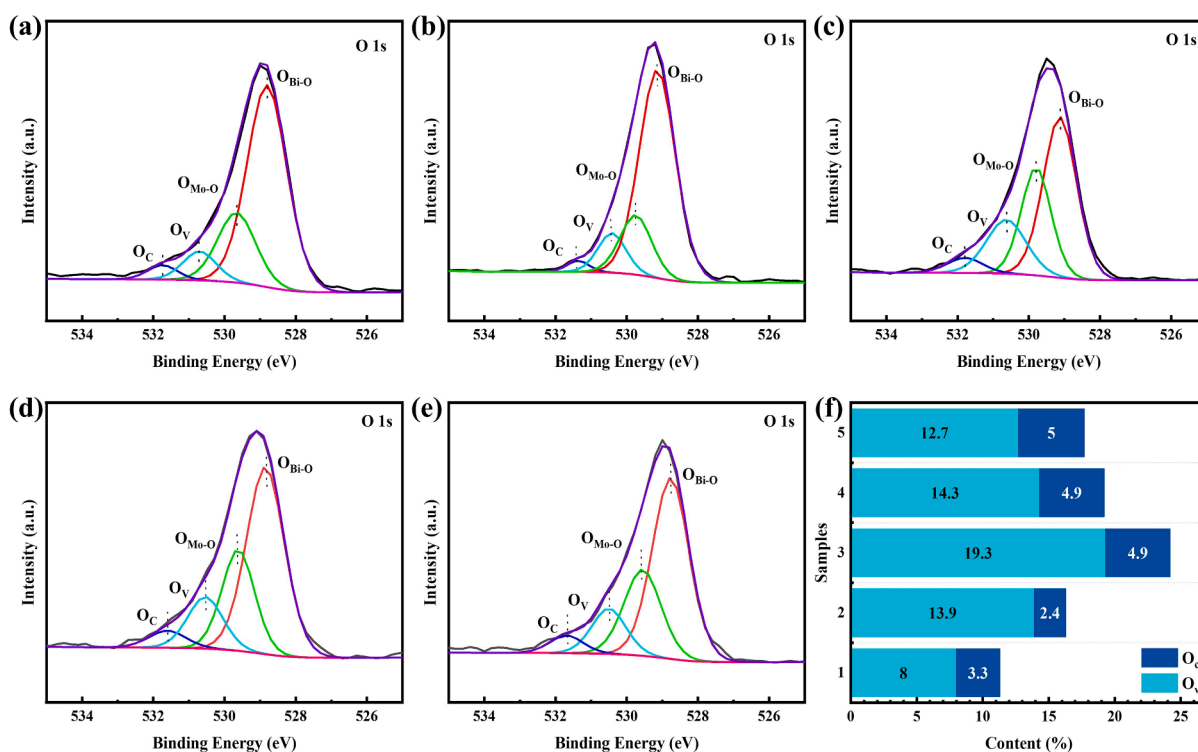

Fig. 7. High-resolution O 1s spectra of a) pristine Bi_2MoO_6, b) 0.5 wt% E-g-C_3N_4/Bi_2MoO_6, c) 1 wt% E-g-C_3N_4/Bi_2MoO_6, d) 3 wt% E-g-C_3N_4/Bi_2MoO_6 and e) 5 wt% E-g-C_3N_4/Bi_2MoO_6. f) Oxygen species content ($O_v + O_c$) of pristine Bi_2MoO_6 (1) and all E-g-C_3N_4/Bi_2MoO_6 composites samples (2–5).
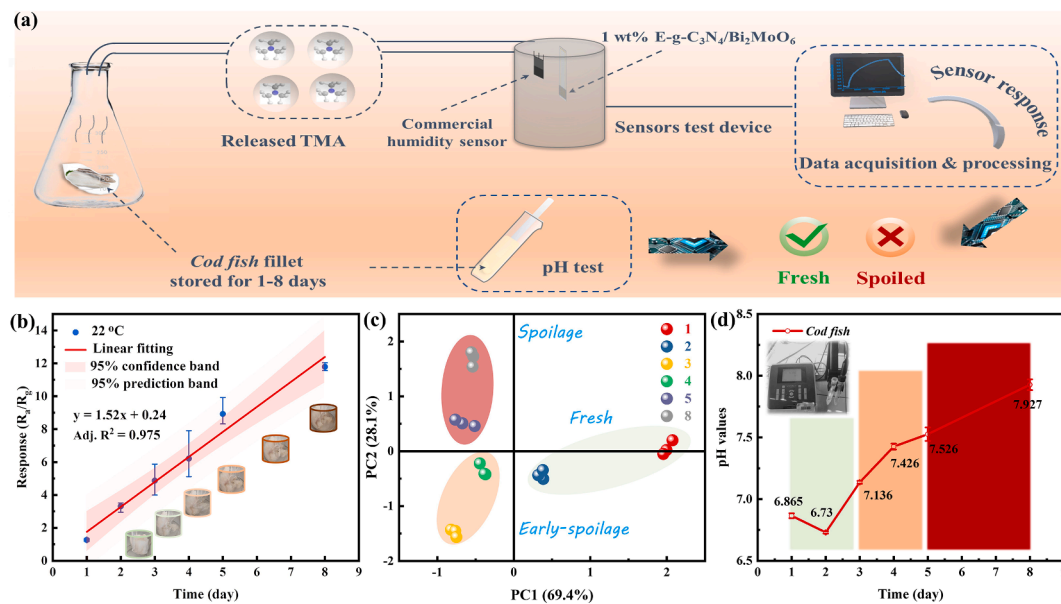
Fig. 8. (a) Block diagram of the fish freshness evaluation system. (b) Linear response of 1 wt% E-g-C_3N_4/Bi_2MoO_6 to the spoilage volatile gas of fish stored for 1–8 days at 23 °C. (c) PCA analysis of the detection results. (d) Real-time pH analysis of the fish stored for 1–8 days.

on Day 3–8, the pH gradually increased from 7.136 to 7.927, which was ascribed to the spoilage decomposition of protein and the production of alkaline metabolites [53,54]. Based on the sensor response, pH values and physical properties change of fish, we used the PCA pattern to classify the fish with various freshness states. In PCA, the response values, baseline resistance and stable resistance values in target gas were used to carry out the principal component analysis. As shown in Fig. 8c, the first PC represented 69.4% of the information content contained in the data, while the second was 28.1%. And the fish kept fresh for two days, the fish on the 3rd and 4th days belong to the early spoilage stage, and the fish on the 5th and 8th days completely deteriorated. Therefore, the application results confirmed the rapid and non-destructive fish freshness detection of 1 wt% E-g-C_3N_4/Bi_2MoO_6 gas sensor.

Additionally, the effect of storage temperature of fish on the response was also investigated. Fig. S11 showed the results of the sensor detecting Cod stored at −4 °C. The sensor response values to Cod stored for 28 days at − 4 °C were 1.24, 1.25, 1.33 and 2.02. It is obvious that the *Cod* fish was still fresh after 28 days.

4. Conclusions

In this work, we developed simple chemiresistive-type gas sensors based on Aurivillius oxide composite microspheres (Bi_2MoO_6 and E-g-C_3N_4/Bi_2MoO_6) using a facile solvothermal synthesis method. Among the nanocomposites, 1 wt% E-g-C_3N_4/Bi_2MoO_6 composites displayed the best sensing properties towards 5–20 ppm TMA, including superior response (R_a/R_g = 10.6 @ 20 ppm), fine selectivity, low detection limit (1.3 ppm), and repeatability. The excellent gas sensing performance was enabled by the synergetic effect of unique micro-nanostructure, crystal defects, and n-n heterojunction structure. Moreover, the 1 wt% E-g-C_3N_4/Bi_2MoO_6 sensor was utilized to detect the freshness of *Cod* fish (1–8 days) and its practicability was verified. Hence, this work could serve as a reference on how to prepare high-performance gas sensors or devices with low power consumption and valid practicality.

CRediT authorship contribution statement

Kaidi Wu: Conceptualization, Methodology, Investigation, Writing – original draft, Writing – review & editing. **Xiaoxi He:** Investigation. **Ahmadou Ly:** Methodology, Investigation. **Driss Lahem:** Methodology,

Investigation. **Marc Debliquy:** Writing – review & editing. **Chao Zhang:** Supervision, Funding acquisition, Resources, Writing – review & editing.

Declaration of Competing Interest

The authors declare that they have no known competing financial interests or personal relationships that could have appeared to influence the work reported in this paper.

Data availability

Data will be made available on request.

Appendix A. Supplementary data

Supplementary data to this article can be found online at https://doi.org/10.1016/j.apsusc.2023.157443.

References

[1] S. Zhuang, H. Hong, L. Zhang, Y. Luo, Spoilage-related microbiota in fish and crustaceans during storage: Research progress and future trends, Compr. Rev. Food Sci. Food Saf. 20 (2021) 252–288, https://doi.org/10.1111/1541-4337.12659.

[2] X. Liu, K. Chen, J. Wang, Y. Wang, Y. Tang, X. Gao, L. Zhu, X. Li, J. Li, An on-package colorimetric sensing label based on a sol-gel matrix for fish freshness monitoring, Food Chem. 307 (2020), 125580, https://doi.org/10.1016/j.foodchem.2019.125580.

[3] A.Y. Khaled, C.A. Parrish, A. Adedeji, Emerging nondestructive approaches for meat quality and safety evaluation—A review, Compr. Rev. Food Sci. Food Saf. 20 (2021) 3438–3463, https://doi.org/10.1111/1541-4337.12781.

[4] L. Wu, H. Pu, D.-W. Sun, Novel techniques for evaluating freshness quality attributes of fish: A review of recent developments, Trends Food Sci. Technol. 83 (2019) 259–273, https://doi.org/10.1016/j.tifs.2018.12.002.

[5] K. Mitsubayashi, Y. Kubotera, K. Yano, Y. Hashimoto, T. Kon, S. Nakakura, Y. Nishi, H. Endo, Trimethylamine biosensor with flavin-containing monooxygenase type 3 (FMO3) for fish-freshness analysis, Sens. Actuators B Chem. 103 (2004) 463–467, https://doi.org/10.1016/j.snb.2004.05.006.

[6] D. Wu, M. Zhang, H. Chen, B. Bhandari, Freshness monitoring technology of fish products in intelligent packaging, Crit. Rev. Food Sci. Nutr. 61 (2021) 1279–1292, https://doi.org/10.1080/10408398.2020.1757615.

[7] P.K. Prabhakar, S. Vatsa, P.P. Srivastav, S.S. Pathak, A comprehensive review on freshness of fish and assessment: Analytical methods and recent innovations, Food Res. Int. 133 (2020), 109157, https://doi.org/10.1016/j.foodres.2020.109157.

[8] A.K. Diallo, J. Tardy, Z.Q. Zhang, F. Bessueille, N. Jaffrezic-Renault, M. Lemiti, Trimethylamine biosensor based on pentacene enzymatic organic field effect transistor, Appl. Phys. Lett. 94 (2009), 263302, https://doi.org/10.1063/1.3167805.

[9] S. Shen, X. Zhang, X. Cheng, Y. Xu, S. Gao, H. Zhao, X. Zhou, L. Huo, Oxygen-vacancy-enriched porous α-MoO₃ nanosheet for trimethylamine sensing, ACS Appl. Nano Mater. 2 (2019) 8016–8026, https://doi.org/10.1021/acsanm.9b02072.

[10] T. Dai, Z. Yan, M. Li, Y. Han, Z. Deng, S. Wang, R. Wang, X. Xu, L. Shi, W. Tong, J. Bao, Z. Qiao, L. Li, G. Meng, Boosting electrical response toward trace volatile organic compounds molecules via pulsed temperature modulation of Pt anchored WO₃ chemiresistor, Small Methods. n/a (n.d.) 2200728. 10.1002/smtd.202200728.

[11] J. Shen, S. Xu, C. Zhao, X. Qiao, H. Liu, Y. Zhao, J. Wei, Y. Zhu, Bimetallic Au@Pt nanocrystal sensitization mesoporous α-Fe₂O₃ hollow nanocubes for highly sensitive and rapid detection of fish freshness at low temperature, ACS Appl. Mater. Interfaces 13 (2021) 57597–57608, https://doi.org/10.1021/acsami.1c17695.

[12] Y. Li, B. Liu, H. Wang, X. Su, L. Gao, F. Zhou, G. Duan, Co₃O₄ nanosheet-built hollow dodecahedrons via a two-step self-templated method and their multifunctional applications, Sci. China Mater. 61 (2018) 1575–1586, https://doi.org/10.1007/s40843-018-9254-6.

[13] D. Meng, T. Qiao, G. Wang, Y. Shen, X. San, Y. Pan, F. Meng, NiO-functionalized In₂O₃ flower-like structures with enhanced trimethylamine gas sensing performance, Appl. Surf. Sci. 577 (2022), 151877, https://doi.org/10.1016/j.apsusc.2021.151877.

[14] Z. Li, H. Li, Z. Wu, M. Wang, J. Luo, H. Torun, P. Hu, C. Yang, M. Grundmann, X. Liu, Y. Fu, Advances in designs and mechanisms of semiconducting metal oxide nanostructures for high-precision gas sensors operated at room temperature, Mater. Horiz. 6 (2019) 470–506, https://doi.org/10.1039/C8MH01365A.

[15] S. Das, S. Mojumder, D. Saha, M. Pal, Influence of major parameters on the sensing mechanism of semiconductor metal oxide based chemiresistive gas sensors: A review focused on personalized healthcare, Sens. Actuators B: Chem. 352 (2022), 131066, https://doi.org/10.1016/j.snb.2021.131066.

[16] A. Singh, S. Sikarwar, A. Verma, B. Chandra Yadav, The recent development of metal oxide heterostructures based gas sensor, their future opportunities and challenges: A review, Sens. Actuators Phys. 332 (2021), 113127, https://doi.org/10.1016/j.sna.2021.113127.

[17] B. Mondal, P.K. Gogoi, Nanoscale heterostructured materials based on metal oxides for a chemiresistive gas sensor, ACS Appl. Electron. Mater. 4 (2022) 59–86, https://doi.org/10.1021/acsaelm.1c00841.

[18] J. Bruce, K. Bosnick, E. Kamali Heidari, Pd-decorated ZnO nanoflowers as a promising gas sensor for the detection of meat spoilage, Sens. Actuators B Chem. 355 (2022), 131316, https://doi.org/10.1016/j.snb.2021.131316.

[19] L. He, H. Lv, L. Ma, W. Li, J. Si, M. Ikram, M. Ullah, H. Wu, R. Wang, K. Shi, Controllable synthesis of intercalated γ-Bi₂MoO₆/graphene nanosheet composites for high performance NO₂ gas sensor at room temperature, Carbon. 157 (2020) 22–32, https://doi.org/10.1016/j.carbon.2019.10.011.

[20] S. Liu, Y. Qin, Y. Bai, Highly response and humidity-resistant gas sensor based on polyaniline-functionalized Bi₂MoO₆ with UV activation, Electrochimica Acta. 427 (2022), 140863, https://doi.org/10.1016/j.electacta.2022.140863.

[21] M. Ullah, H. Lv, Z. Liu, X. Bai, J. Chen, Y. Zhang, J. Wang, B. Sun, L. Li, K. Shi, Rational fabrication of a g-C₃N₄/NiO hierarchical nanocomposite with a large surface area for the effective detection of NO₂ gas at room temperature, Appl. Surf. Sci. 550 (2021) 149368, https://doi.org/10.1016/j.apsusc.2021.149368.

[22] M. Chen, Y. Jia, H. Li, Z. Wu, T. Huang, H. Zhang, Enhanced pyrocatalysis of the pyroelectric BiFeO₃/g-C₃N₄ heterostructure for dye decomposition driven by cold-hot temperature alternation, J. Adv. Ceram. 10 (2021) 338–346, https://doi.org/10.1007/s40145-020-0446-x.

[23] M. Reddeppa, N.T. KimPhung, G. Murali, K.S. Pasupuleti, B.-G. Park, I. In, M.-D. Kim, Interaction activated interfacial charge transfer in 2D g-C₃N₄/GaN nanorods heterostructure for self-powered UV photodetector and room temperature NO₂ gas sensor at ppb level, Sens. Actuators B Chem. 329 (2021), 129175, https://doi.org/10.1016/j.snb.2020.129175.

[24] D. Wang, S. Huang, H. Li, A. Chen, P. Wang, J. Yang, X. Wang, J. Yang, Ultrathin WO₃ nanosheets modified by g-C₃N₄ for highly efficient acetone vapor detection, Sens. Actuators B Chem. 282 (2019) 961–971, https://doi.org/10.1016/j.snb.2018.11.138.

[25] Z.-H. Yu, Y.-L. Gan, J. Xu, B. Xue, Direct catalytic hydroxylation of benzene to phenol catalyzed by FeCl₃ supported on exfoliated graphitic carbon nitride, Catal. Lett. 150 (2020) 301–311, https://doi.org/10.1007/s10562-019-03003-2.

[26] Y.-J. Yuan, Z. Shen, S. Wu, Y. Su, L. Pei, Z. Ji, M. Ding, W. Bai, Y. Chen, Z.-T. Yu, Z. Zou, Liquid exfoliation of g-C₃N₄ nanosheets to construct 2D–2D MoS₂/g-C₃N₄

photocatalyst for enhanced photocatalytic H₂ production activity, Appl. Catal. B Environ. 246 (2019) 120–128, https://doi.org/10.1016/j.apcatb.2019.01.043.

[27] N.T. Hang, S. Zhang, W. Yang, Efficient exfoliation of g-C₃N₄ and NO₂ sensing behavior of graphene/g-C₃N₄ nanocomposite, Sens. Actuators B Chem. 248 (2017) 940–948, https://doi.org/10.1016/j.snb.2017.01.199.

[28] K. Zhao, Z. Zhang, Y. Feng, S. Lin, H. Li, X. Gao, Surface oxygen vacancy modified Bi₂MoO₆/MIL-88B(Fe) heterostructure with enhanced spatial charge separation at the bulk & interface, Appl. Catal. B Environ. 268 (2020), 118740, https://doi.org/10.1016/j.apcatb.2020.118740.

[29] S. Li, C. Wang, M. Cai, Y. Liu, K. Dong, J. Zhang, Designing oxygen vacancy mediated bismuth molybdate (Bi₂MoO₆)/N-rich carbon nitride (C₃N₅) S-scheme heterojunctions for boosted photocatalytic removal of tetracycline antibiotic and Cr(VI): Intermediate toxicity and mechanism insight, J. Colloid Interface Sci. 624 (2022) 219–232, https://doi.org/10.1016/j.jcis.2022.05.151.

[30] F. Yakuphanoglu, Electrical characterization and device characterization of ZnO microring shaped films by sol–gel method, J. Alloys Compd. 507 (2010) 184–189, https://doi.org/10.1016/j.jallcom.2010.07.151.

[31] B. Yu, Y. Wu, F. Meng, Q. Wang, X. Jia, M. Wasim Khan, C. Huang, S. Zhang, L. Yang, H. Wu, Formation of hierarchical Bi₂MoO₆/ln₂S₃ S-scheme heterojunction with rich oxygen vacancies for boosting photocatalytic CO₂ reduction, Chem. Eng. J. 429 (2022), 132456, https://doi.org/10.1016/j.cej.2021.132456.

[32] M. Vila, C. Díaz-Guerra, K. Lorenz, J. Piqueras, E. Alves, S. Nappini, E. Magnano, Structural and luminescence properties of Eu and Er implanted Bi₂O₃ nanowires for optoelectronic applications, J. Mater. Chem. C. 1 (2013) 7920–7929, https://doi.org/10.1039/C3TC31989J.

[33] A. Yousif, R.M. Jafer, S. Som, M.M. Duvenhage, E. Coetsee, H.C. Swart, Ultra-broadband luminescent from a Bi doped CaO matrix, RSC Adv. 5 (2015) 54115–54122, https://doi.org/10.1039/C5RA09246A.

[34] W. Dai, J. Long, L. Yang, S. Zhang, Y. Xu, X. Luo, J. Zou, S. Luo, Oxygen migration triggering molybdenum exposure in oxygen vacancy-rich ultra-thin Bi₂MoO₆ nanoflakes: Dual binding sites governing selective CO₂ reduction into liquid hydrocarbons, J. Energy Chem. 61 (2021) 281–289, https://doi.org/10.1016/j.jechem.2021.01.009.

[35] W. Yan, L. Yan, C. Jing, Impact of doped metals on urea-derived g-C₃N₄ for photocatalytic degradation of antibiotics: Structure, photoactivity and degradation mechanisms, Appl. Catal. B Environ. 244 (2019) 475–485, https://doi.org/10.1016/j.apcatb.2018.11.069.

[36] Z. Zhang, C. Liu, Z. Dong, Y. Dai, G. Xiong, Y. Liu, Y. Wang, Y. Wang, Y. Liu, Synthesis of flower-like MoS₂/g-C₃N₄ nanosheet heterojunctions with enhanced photocatalytic reduction activity of uranium(VI), Appl. Surf. Sci. 520 (2020), 146352, https://doi.org/10.1016/j.apsusc.2020.146352.

[37] Y. Huang, B. Chen, J. Duan, F. Yang, T. Wang, Z. Wang, W. Yang, C. Hu, W. Luo, Y. Huang, Graphitic carbon nitride (g-C₃N₄): An interface enabler for solid-state lithium metal batteries, Angew. Chem. 132 (2020) 3728–3733, https://doi.org/10.1002/ange.201914417.

[38] Y. Deng, J. Liu, Y. Huang, M. Ma, K. Liu, X. Dou, Z. Wang, S. Qu, Z. Wang, Engineering the photocatalytic behaviors of g/C₃N₄-based metal-free materials for degradation of a representative antibiotic, Adv. Funct. Mater. 30 (2020) 2002353, https://doi.org/10.1002/adfm.202002353.

[39] D. Meng, R. Li, L. Zhang, G. Wang, Y. Zhang, X. San, X. Wang, Synthesis of NiMoO₄-functionalized MoO₃ nanorods with enhanced TMA gas sensing properties, Sensors and Actuators Reports. 4 (2022), 100104, https://doi.org/10.1016/j.snr.2022.100104.

[40] D.-X. Ju, H.-Y. Xu, Z.-W. Qiu, Z.-C. Zhang, Q. Xu, J. Zhang, J.-Q. Wang, B.-Q. Cao, Near room temperature, Fast-response, and highly sensitive triethylamine sensor assembled with Au-loaded ZnO/SnO₂ core–shell nanorods on flat alumina substrates, ACS Appl. Mater. Interfaces. 7 (2015) 19163–19171, https://doi.org/10.1021/acsami.5b04904.

[41] F. Zhang, K. Liu, H. Li, S. Cui, D. Zhang, J. Zeng, Z. Yan, MoO₃ nanorods decorated by PbMoO₄ nanoparticles for enhanced trimethylamine sensing performances at low working temperature, ACS Appl. Mater. Interfaces. 14 (2022) 24610–24619, https://doi.org/10.1021/acsami.2c04722.

[42] Y. Liu, X. Li, X. Li, C. Shao, C. Han, J. Xin, D. Lu, L. Niu, Y. Tang, Y. Liu, Highly permeable WO₃/CuWO₄ heterostructure with 3D hierarchical porous structure for high-sensitive room-temperature visible-light driven gas sensor, Sens. Actuators B Chem. 365 (2022) 131926, https://doi.org/10.1016/j.snb.2022.131926.

[43] J. Lee, Y. Choi, B.J. Park, J.W. Han, H.-S. Lee, J.H. Park, W. Lee, Precise control of surface oxygen vacancies in ZnO nanoparticles for extremely high acetone sensing response, J. Adv. Ceram. 11 (2022) 769–783, https://doi.org/10.1007/s40145-022-0570-x.

[44] C. Zhang, K. Wu, H. Liao, M. Debliquy, Room temperature WO₃-Bi₂WO₆ sensors based on hierarchical microflowers for ppb-level H₂S detection, Chem. Eng. J. 430 (2022), 132813, https://doi.org/10.1016/j.cej.2021.132813.

[45] D. Zhao, X. Zhang, W. Wang, L. Sui, C. Guo, Y. Xu, X. Zhou, X. Cheng, S. Gao, L. Huo, Synthesis of enriched oxygen vacancy TiO₂ microsphere with rapid response to isopropylamine and its application in herbicide detection, Sens. Actuators B: Chem. 370 (2022), 132423.

[46] K. Wu, W. Zhang, Z. Zheng, M. Debliquy, C. Zhang, Room-temperature gas sensors based on titanium dioxide quantum dots for highly sensitive and selective H₂S detection, Appl. Surf. Sci. 585 (2022), 152744, https://doi.org/10.1016/j.apsusc.2022.152744.

[47] W. Yan, H. Xu, M. Ling, S. Zhou, T. Qiu, Y. Deng, Z. Zhao, E. Zhang, MOF-Derived Porous Hollow Co₃O₄@ZnO Cages for High-Performance MEMS Trimethylamine Sensors, ACS Sens. 6 (2021) 2613–2621, https://doi.org/10.1021/acssensors.1c00315.

[48] R. Pandeeswari, B.G. Jeyaprakash, Nanostructured α-MoO$_3$ thin film as a highly selective TMA sensor, Biosens. Bioelectron. 53 (2014) 182–186, https://doi.org/10.1016/j.bios.2013.09.057.

[49] C. Li, P.G. Choi, Y. Masuda, Highly sensitive and selective gas sensors based on NiO/MnO$_2$@NiO nanosheets to detect allyl mercaptan gas released by humans under psychological stress, Adv. Sci. 9 (2022) 2202442, https://doi.org/10.1002/advs.202202442.

[50] X. Sun, R. Gao, Y. Wu, X. Zhang, X. Cheng, S. Gao, Y. Xu, L. Huo, Novel in-situ deposited V$_2$O$_5$ nanorods array film sensor with enhanced gas sensing performance to n-butylamine, Chem. Eng. J. 459 (2023), 141505, https://doi.org/10.1016/j.cej.2023.141505.

[51] F. Xu, J. Wang, N. Zhang, H. Liang, H. Sun, Simultaneously generating Bi quantum dot and oxygen vacancy on Bi$_2$MoO$_6$ nanosheets for boosting photocatalytic

[52] K. Wu, M. Debliquy, C. Zhang, Room temperature gas sensors based on Ce doped TiO$_2$ nanocrystals for highly sensitive NH3 detection, Chem. Eng. J. 444 (2022), 136449, https://doi.org/10.1016/j.cej.2022.136449.

[53] S. Fang, Z. Guan, C. Su, W. Zhang, J. Zhu, Y. Zheng, H. Li, P. Zhao, X. Liu, Accurate fish-freshness prediction label based on red cabbage anthocyanins, Food Control. 138 (2022), 109018, https://doi.org/10.1016/j.foodcont.2022.109018.

[54] Z. Teymouri, H. Shekarchizadeh, A colorimetric indicator based on copper nanoparticles for volatile sulfur compounds to monitor fish spoilage in intelligent packaging, Food Packag. Shelf Life. 33 (2022), 100884, https://doi.org/10.1016/j.fpsl.2022.100884.

selective alcohol oxidation, Appl. Surf. Sci. 575 (2022), 151738, https://doi.org/10.1016/j.apsusc.2021.151738.